

Analysis of scattered waves on ground with irregular  
topography using the direct boundary element method and  
Neumann series expansion

HIDENORI MOGI\* and HIDEJI KAWAKAMI†

\* Department of Civil and Environmental Engineering, Saitama University, Japan.

† Geosphere Research Institute of Saitama University, Japan.

## **Abstract**

It is well known that ground with irregular topographic surfaces causes complicated seismic responses. The cause of the complex seismic response is mainly due to scattering and wave conversions. However, the specific locations of the surface where the scattering mainly occurs and the extent of their effects are not yet clear. In this study, we investigated the excitation process of complicated seismic responses induced by irregular ground surfaces in terms of the contribution of scattered waves. Firstly, the formulation of scattered-wave contribution in a two-dimensional SH wavefield based on the direct boundary element method (BEM) and the Neumann series expansion of the BEM matrix was shown. In the formulation process, it was pointed out that the mathematical expression of the first-order scattered-wave contribution has a form consisting of a wavefunction and an inclination factor, which was similar to that obtained from the Huygens-Fresnel principle. Next, numerical analyses were conducted for a ground that had a sinusoidal-shaped surface at the center and flat parts at both ends. A comparison of the results showed that the complicated waveforms of the responses were caused by the arrivals of the scattered waves. Finally, the contributions of the first-order scattered waves at the reference points were closely examined based on the mathematical expression, and the following conclusions were drawn: (1) The polarity of the first-order scattered waves in the time domain is attributed to the inclination factor, which depends only on the geometrical relationship between the reference point and the source

point where the scattered waves emanate from. (2) At the bottom of a valley, the scattered waves generated at its nearby surface are dominant because of the short distance from the source of the scattered waves. These scattered waves appear nearly at the same time of arrival as the incident wave and always reduce the amplitude of the incident wave due to their negative polarity. (3) On the contrary, at the peak of a hill, the scattered waves generated at the nearby surface have positive polarity, and they always enhance the amplitude response.

## Introduction

It is well known that ground with irregular topographic surfaces causes complicated seismic responses. One of the pioneering works done on this effect is the examination of strong ground motion recorded at Pacoima Dam during the 1971 San Fernando earthquake. Boore (1972, 1973) conducted finite difference analyses of the SH wavefield to evaluate the effects of the irregular topography at the Pacoima Dam area, and showed that the motion at the ridge crest was amplified by the convex ground shape. Bouchon (1973) also discussed the effect of surface topography on the P-SV wavefield as well as the SH wavefield by using the time-domain extension of the Aki-Larner method (Aki and Larner, 1970) and obtained similar results—“the main feature is the existence of an amplification at the top, the value of which ranges from about 50 percent for normal P, normal SV and oblique P (vertical component) to 100 percent for oblique SV (horizontal component).” Since then, many analyses of ground motion in areas with irregular surfaces have been performed: e.g., by the Aki-Larner method (Bard, 1982; Geli *et al.*, 1988); by the boundary element method (Sanchez-Sesma *et al.*, 1982; Kawase, 1988; Sanchez-Sesma and Campillo, 1991; Bouchon *et al.*, 1996; Reinoso *et al.*, 1997); by the finite element method (Ohtsuki and Harumi, 1983); and by analytical approaches to problems with a simple ground shape (Sanchez-Sesma, 1985). In addition to the above numerical “exact” solutions, other methods using approximation techniques have been proposed: e.g., the first-order perturbation technique or the Kirchhoff approximation (Kennet,

1972; Scott and Helmberger, 1983; Frazer and Sinton, 1984; and Zhang and Shinozuka, 1996); and the Neumann series expansion (Hudson and Heritage, 1981; Fujiwara and Takenaka, 1994; Hatayama and Fujiwara, 1998; Mogi *et al.*, 2005; and Fu, 2005). Several state-of-the-art studies in this field were also published (Aki, 1989; and Koketsu and Takenaka, 1989).

These studies have revealed that the complex seismic responses are induced by irregular topography, and the results were discussed based mainly on comparisons between the responses on ground with irregular topography and that without irregularities. However, they do not clarify the cause of the complex response. The complex seismic response is, of course, mainly due to scattering (and wave conversions in a P-SV wavefield). However, the specific locations of the surface where the scattering mainly occurs and the extent of their effects are not yet clear.

The authors previously conducted a frequency-domain analysis in the SH wavefield based on the direct boundary element method (BEM) and the Neumann series expansion of the BEM matrix and showed that the generation of scattered waves could be examined by each term of the Neumann series (Mogi *et al.*, 2005). However, this analysis was in the frequency domain, so the discussion on the interference between an incident wave and the scattered waves was insufficient. In this study, we investigated the excitation process of complicated seismic responses induced by irregular ground surfaces in terms of the scattered-wave contribution in a time domain. Firstly, the formulation of the scattered-wave contribution in a two-dimensional SH wavefield was shown. The contribution represents the amplitude of the waves scattered at each part of the ground

surface and having arrived at a reference point. In the review of the formulation process, it was pointed out that the mathematical expression of the first-order scattered-wave contribution has a form consisting of a wavefunction and an inclination factor, which was similar to that obtained from the Huygens–Fresnel principle. Next, we conducted numerical analyses for ground that had a sinusoidal-shaped surface at the center and flat parts at both ends. In these analyses, the total responses and the contributions of the first- to third-order scattered waves in the time domain at three reference points were evaluated. A comparison of them showed that the complicated waveforms of the responses were caused by the arrival of the scattered waves. It was also shown that the first-order scattered waves dominated the higher-order scattered waves; thus, we can examine the properties of the scattered waves based only on the first-order ones.

Finally, the contributions of the first-order scattered waves at the reference points were closely examined based on the mathematical expression, and the following conclusions were drawn: (1) The polarity of the first-order scattered waves in the time domain is attributed to the inclination factor, which depends only on the geometrical relationship between the reference point and the source point where the scattered waves emanate from. (2) At the bottom of a valley, the scattered waves generated at its nearby surface are dominant over those from the other parts of the surface because of the short distance from the source of the scattered waves. These scattered waves appear nearly at the same time of arrival as the incident wave and always reduce the amplitude of the incident wave due to their negative polarity. (3) On the contrary, at the peak of a

hill, the scattered waves generated at the nearby surface have positive polarity, and they always enhance the amplitude response.

## Analysis Method

### Boundary Integral Equation

In this section we outline the boundary element method (BEM). Further details can be found in textbooks (e.g., Brebbia and Walker, 1980 and Kobayashi, 1985).

Consider a two-dimensional ground model with an irregular surface, as shown in figure 1.

Displacements of SH-waves with harmonic time-dependence of angular frequency  $\omega$ ,  $\exp(i\omega t)$ , satisfy the Helmholtz equation

$$\{\nabla^2 + k_\beta^2\} u(\mathbf{X}) = 0, \quad (1)$$

where  $u(\mathbf{X})$  is the displacement at arbitrary point  $\mathbf{X} = (x, z)$ ,  $k_\beta = \omega/\beta$  is the wavenumber of the S-wave, and  $\beta$  is the S-wave velocity.

From equation (1), the following boundary integral equation can be obtained:

$$\frac{1}{2} u(\mathbf{Y}) + \text{v.p.} \int_\Gamma q^*(\mathbf{X}, \mathbf{Y}) u(\mathbf{X}) d\Gamma(\mathbf{X}) - \int_\Gamma u^*(\mathbf{X}, \mathbf{Y}) q(\mathbf{X}) d\Gamma(\mathbf{X}) = v(\mathbf{Y}), \quad (2)$$

where  $\mathbf{X}$  and  $\mathbf{Y}$  are points on boundary  $\Gamma$ , v.p. is the Cauchy principal-value integral,  $v(\mathbf{Y})$  is the displacement of the incident wave, and  $q(\mathbf{X})$  is the gradient of  $u(\mathbf{X})$  in the normal direction

$n$ . Fundamental solutions  $u^*(\mathbf{X}, \mathbf{Y})$  and  $q^*(\mathbf{X}, \mathbf{Y})$  in equation (2) are given by

$$\begin{aligned} u^*(\mathbf{X}, \mathbf{Y}) &= -\frac{i}{4} H_0^{(2)}(k_\beta r), \\ q^*(\mathbf{X}, \mathbf{Y}) &= \frac{\partial u^*(\mathbf{X}, \mathbf{Y})}{\partial \mathbf{n}(\mathbf{X})} = \frac{ik_\beta}{4} H_1^{(2)}(k_\beta r) \frac{\partial r}{\partial \mathbf{n}(\mathbf{X})}, \end{aligned} \quad (3)$$

where  $r$  is the distance between  $\mathbf{X}$  and  $\mathbf{Y}$ , and  $H_\nu^{(2)}(\cdot)$  is the Hankel function of the second kind of order  $\nu$  (e.g., Brebbia and Walker, 1980). Because the homogeneous ground with free surface ( $q(\mathbf{X})=0, \mathbf{X} \in \Gamma$ ) is considered, equation (2) is simplified as follows:

$$\frac{1}{2} u(\mathbf{Y}) + \text{v.p.} \int_\Gamma q^*(\mathbf{X}, \mathbf{Y}) u(\mathbf{X}) d\Gamma(\mathbf{X}) = v(\mathbf{Y}). \quad (4)$$

### Discretization of Boundary Integral Equation

For the numerical solution of the boundary integral equation (4), boundary  $\Gamma$  is divided into  $J$  elements  $\Gamma_j, (j = 1, \dots, J)$ . We assume that  $u(\mathbf{Y})$  and  $v(\mathbf{Y})$  are piecewise constant on the boundary, and that they can be expressed as nodal boundary values

$$\begin{aligned} \mathbf{u}(\mathbf{Y}) &= \{u(\mathbf{Y}_1), \dots, u(\mathbf{Y}_J)\}^T, \\ \mathbf{v}(\mathbf{Y}) &= \{v(\mathbf{Y}_1), \dots, v(\mathbf{Y}_J)\}^T, \end{aligned} \quad (5)$$

where  $\mathbf{Y}_j$  is the midpoint of boundary element  $\Gamma_j$ . Using the nodal values, equation (4) can be discretized as

$$\frac{1}{2} u(\mathbf{Y}_j) + \sum_{m=1}^J u(\mathbf{X}_m) \int_{\Gamma_m} q^*(\mathbf{X}, \mathbf{Y}_j) d\Gamma(\mathbf{X})$$

$$= \frac{1}{2} \sum_{m=1}^J u(\mathbf{X}_m) h'_{jm} = v(\mathbf{Y}_j). \quad (6)$$

The term  $h'_{jm}$  in equation (6) is the boundary integral of  $q^*(\mathbf{X}, \mathbf{Y}_j)$  on  $\Gamma_m$  and is given by

$$\begin{aligned} h'_{jm} &= 2 \int_{\Gamma_m} q^*(\mathbf{X}, \mathbf{Y}_j) d\Gamma(\mathbf{X}) + \delta_{jm} \\ &= 2 \int_{\Gamma_m} \frac{ik_\beta}{4} H_1^{(2)}(k_\beta r) \frac{\partial r}{\partial \mathbf{n}(\mathbf{X})} d\Gamma(\mathbf{X}) + \delta_{jm} \end{aligned} \quad (7)$$

where  $\delta_{jm}$  is the Kronecker delta.

The integration in equation (7) has to be performed as a Cauchy principal-value integral for the case of  $j = m$ . In linear-segment element discretization, however, the integrand in equation (7) vanishes for  $j = m$  because of  $\partial r / \partial \mathbf{n} = 0$ , so that we get

$$h'_{jj} = \delta_{jj} = 1. \quad (8)$$

By the forementioned discretization of equation (6), we get the following simultaneous equations:

$$\mathbf{v} = \frac{1}{2} \mathbf{H}' \mathbf{u} \quad (9)$$

where  $\mathbf{H}'$  is the boundary element matrix whose elements are given in equation (7).

## Two Solutions of the Simultaneous Equations

### *Exact Numerical Solution*

In the conventional BEM, equation (9) is solved numerically. Furthermore, the following modification is possible:

$$\mathbf{u} = \mathbf{H}'^{-1}2\mathbf{v} = \mathbf{E}2\mathbf{v} + \mathbf{S}2\mathbf{v} = \mathbf{E}2\mathbf{v} + \mathbf{u}^s, \quad (10)$$

where

$$\mathbf{S} = \mathbf{H}'^{-1} - \mathbf{E}, \quad (11)$$

$$\mathbf{u}^s = \mathbf{S}2\mathbf{v}, \quad (12)$$

and  $\mathbf{E}$  is a unit matrix. The first term on the right side of equation (10),  $\mathbf{E}2\mathbf{v}$ , can be understood as the displacements directly caused by an incident wave (i.e., its amplitude is twice that of the incident wave), and the second term,  $\mathbf{S}2\mathbf{v}$  or  $\mathbf{u}^s$ , represents the displacements induced by the scattered waves (including multiple scattering) generated at the irregular ground surface.

*Approximate Solution by Neumann Series Expansion of the Boundary Element Matrix*

The inverse matrix of square matrix  $\mathbf{A} = \mathbf{E} - \mathbf{T}$  can be given by using  $\mathbf{T}$  as

$$\mathbf{A}^{-1} = (\mathbf{E} - \mathbf{T})^{-1} = \sum_{n=0}^{\infty} \mathbf{T}^n, \quad (13)$$

where  $\mathbf{E}$  is a unit matrix (e.g., Kato, 1980). The series in equation (13) is called the Neumann series, and is absolutely convergent for  $\|\mathbf{T}\| < 1$  in virtue of  $\|\mathbf{T}^n\| \leq \|\mathbf{T}\|^n$ . This expansion is also called the Born approximation and has been applied to earthquake-related problems by many researchers (e.g., Hudson *et al.*, 1981; Fujiwara and Takenaka, 1994; Hatayama *et al.*, 1998; Fu, 2005).

We introduce square matrix  $\mathbf{H}$ , which satisfies  $\mathbf{H}' = \mathbf{E} - \mathbf{H}$ . From equations (7) and (8), the non-diagonal elements of  $\mathbf{H}$  are given by

$$h_{jm} = -2 \int_{\Gamma_m} \frac{ik_{\beta}}{4} H_1^{(2)}(k_{\beta}r) \frac{\partial r}{\partial \mathbf{n}(\mathbf{X})} d\Gamma(\mathbf{X}), \quad (14)$$

while the diagonal components are zero.

Applying the Neumann series expansion to equation (9), the unknown displacement  $\mathbf{u}$  can be solved in a different form from equation (10), as

$$\begin{aligned} \mathbf{u} &= (\mathbf{E} - \mathbf{H})^{-1} 2\mathbf{v} \\ &= (\mathbf{E} + \mathbf{H} + \mathbf{H}^2 + \dots) 2\mathbf{v} \\ &= \mathbf{u}^{(0)} + \mathbf{u}^{(1)} + \mathbf{u}^{(2)} + \dots, \end{aligned} \quad (15)$$

where

$$\mathbf{u}^{(\nu)} = \mathbf{H}^\nu \mathbf{2v}, \quad \nu = 0, 1, 2, \dots \quad (16)$$

The first term of the series,  $\mathbf{2Ev}$  or  $\mathbf{u}^{(0)}$ , represents the zeroth order of the series expansion and the incident waves doubled by the ground surface (i.e., without scattered waves). The second term,  $\mathbf{2Hv}$  or  $\mathbf{u}^{(1)}$ , can be understood as the first-order scattered wave, because the integral kernels of the elements of  $\mathbf{H}$  are the Green's function for the reference point  $\mathbf{Y}$  and the source point  $\mathbf{X}$  as shown in equation (14), and because this term represents the responses to the cylindrical waves coming from the other parts of the ground surface. Taking into account that the third term can be written as  $\mathbf{H}^2 \mathbf{2v} = \mathbf{H}(\mathbf{H} \mathbf{2v})$ , it can be similarly understood that the third term represents the responses to the scattered waves reflected twice at the surface. Thus, the order of terms in the series,  $\nu$ , can be considered as the number of surface reflections, and hereafter we refer to  $\nu$  as the order of scattered waves. It should be noted that the greater the topographical irregularity is, the larger the amplitude of the first-order scattered waves becomes, and the higher-order scattered waves may not be negligible.

### Contribution of Scattered Waves

The term  $\mathbf{u}^{(\nu)}$  in equation (15) represents the  $\nu$ -th scattered waves at the ground surface, and the integral kernels of the elements of  $\mathbf{H}$  are the Green's function for the reference point  $\mathbf{Y}$  and

the source point  $X$ , so that the  $(j, m)$  element of  $\mathbf{H}^\nu$  represents the contribution of the  $\nu$ -th order scattered wave from the  $m$ -th element (we refer to it as a source element) to the  $j$ -th node (reference node). Similarly, the  $(j, m)$  element of  $\mathbf{S}$  in equation (11) represents the contribution of all orders of the scattered waves. The length of the source element  $dL_m$ , however, affects the contribution because the energy of an incident wave at each element is proportional to its element length. To avoid this effect, the following normalization was used for the definition of the  $\nu$ -th order scattered-wave contribution from the  $m$ -th element to the  $j$ -th node:

$$\hat{u}_{jm}^{(\nu)} = 2(\mathbf{H}^\nu)_{jm} \frac{v_m}{dL_m}, \quad (17)$$

where  $(\mathbf{H}^\nu)_{jm}$  and  $v_m$  represent the  $(j, m)$  element of  $\mathbf{H}^\nu$  and  $m$  element of  $\mathbf{v}$ . Similarly, the normalized total contribution of scattered waves can be defined as

$$\hat{u}_{jm}^s = 2\mathbf{S}_{jm} \frac{v_m}{dL_m}. \quad (18)$$

For simplicity of expression, we refer to  $\hat{u}_{jm}^{(\nu)}$  and  $\hat{u}_{jm}^s$  as the  $\nu$ -th order scattered wave and the total scattered wave, respectively.

### **Inclination Factor**

The mathematical expression of the first-order scattered wave given by equation (14) has two major factors in its integrand:  $-iH_1^{(2)}(k_\beta r)$  and  $\partial r / \partial \mathbf{n}(\mathbf{X})$ . The former factor represents a

cylindrical wave propagating from the source node where the incident wave impinges; therefore, this cylindrical wave can be understood as being similar to the secondary wavelet in the Huygens-Fresnel principle (e.g., Hecht, 2002). The latter plays a similar role to the inclination factor also incorporated in the Huygens-Fresnel principle; namely, it gives the amplitude of the secondary wavelet propagating in each direction. Considering this similarity of mathematical expression, we refer to this factor,  $\partial r / \partial \mathbf{n}(\mathbf{X})$ , as the inclination factor.

### Polarity of the Scattered Wave

The waveform of the first-order scattered wave at the  $j$ -th node coming from the  $m$ -th element can be estimated by the inverse Fourier transform as

$$\hat{U}_{jm}^{(1)}(t) = \int_{-\infty}^{\infty} \hat{u}_{jm}^{(1)}(\omega) \exp(i\omega t) d\omega = 2 \int_{-\infty}^{\infty} \frac{h_{jm}(\omega)}{dL_m} v_m(\omega) \exp(i\omega t) d\omega. \quad (19)$$

Taking into account that the integrand of  $h_{jm}$  given by equation (14) can be written by using the Bessel functions of order one,  $J_1(\cdot)$  and  $Y_1(\cdot)$ , as

$$-\frac{ik_\beta}{2} H_1^{(2)}(k_\beta r) \frac{\partial r}{\partial \mathbf{n}(\mathbf{X})} = \frac{k_\beta}{2} \{-Y_1(k_\beta r) - iJ_1(k_\beta r)\} \frac{\partial r}{\partial \mathbf{n}(\mathbf{X})}, \quad (20)$$

the polarity of the first-order scattered wave emanating from source node  $\mathbf{X}_m$  can be examined by putting  $r \ll 1$ . For example, for reference point  $\mathbf{Y}_j$  and source point  $\mathbf{X}_m$  located on concave topography as shown in figure 2a, the waveform of the first-order scattered wave at reference point

$Y_j$  has negative polarity (opposite polarity to that of incident wave  $v_m$ ) because equation (20) for  $r \ll 1$  becomes

$$-\frac{ik_\beta}{2}H_1^{(2)}(k_\beta r)\frac{\partial r}{\partial \mathbf{n}(X)} \sim -\frac{k_\beta}{2}Y_1(0)\frac{\partial r}{\partial \mathbf{n}(X)} = -\infty \quad (21)$$

for the negative inclination factor  $\partial r/\partial \mathbf{n}(X)$ . On the contrary, for the points on convex topography (Fig. 2b), the polarity of the first-order scattered wave is positive (same polarity as that of the incident wave) because of their positive inclination factor.

## Preliminary Analysis Based on Conventional BEM

### Ground Model

A ground model with a sinusoidal surface having three reference points A, B, and C is shown in figure 3 in order to examine the characteristic responses of the ground surface. The model was assumed to be an isotropic homogeneous elastic half-space with S-wave velocity of 100 m/s. The length and amplitude of the sinusoidal part are 45 m and 5 m, respectively. The sinusoidal part was discretized with intervals of 0.4 to 0.5 m (95 elements), and the flat parts were discretized with intervals of 2.5 m for  $22.5 \leq |x| < 200$  m (142 elements) and 10 m for  $200 \leq |x| < 600$  m (80 elements); the total number of elements was 317.

## Incident Wave

We used a vertically incident plane SH-wave, with the nodal displacements of the incident wave given by

$$v_m(\omega) = f(\omega) \exp(ik_\beta z_m), \quad (22)$$

where  $f(\omega)$  is the Fourier transform of the time function of the incident wave  $F(t)$ . In the frequency-domain analysis,  $f(\omega)$  in equation (22) was set to unity, and in the time-domain analysis the following Fourier transform of the double-triangular function shown in figure 4a was used:

$$f(\omega) = \frac{2e^{-i\omega T_d}}{\omega^2 T} (1 - \cos \omega T)(1 - e^{-2i\omega T}). \quad (23)$$

The rectilinearity and abrupt change in the shape of the time function in figure 4a can make wave arrivals clear. The spectrum of the incident wave is shown in figure 4b, and the predominant frequency (characterized frequency) given by  $1/(4T)$  is 1.25 Hz.

## Responses at Reference Points

### *Frequency Response*

Figure 5 plots the exact solutions of frequency responses (absolute value) at the three reference points obtained using conventional BEM. In this figure, we can see that the response amplitudes

are very close to 2 for frequencies less than 0.5 Hz. These results can be explained by a long wavelength of a seismic wave for these frequencies. We can also see that the response at the peak (point B) shows amplification over a wide frequency range while the responses at the other points (A and C) vary in the range of 0 to 3.5 depending on frequency. Taking into account the homogeneous ground model, these results show that the effect of topography on ground motion is not negligible.

### *Waveforms*

Figure 6 shows waveforms at various positions obtained using the conventional BEM. The characterized frequency of the incident wave is 1.25 Hz. In this figure, we can see that the response at the trough (point A) has smaller amplitude but a more complicated shape with several bends compared to those at the other locations. These bends can be inferred as the arrivals of scattered waves and will be discussed in detail in a later section. Meanwhile, the waveform at the peak (point B) shows larger amplitude: this result is consistent with previous observations indicating that amplification occurred at the top of a hill or mountain (e.g., Boore, 1972; Boore, 1973; Bouchon, 1973). In flat areas away from irregular surfaces, waveforms are similar to the incident wave shown in figure 4, and the arrivals of scattered waves appear only on the later part of the waveforms (e.g.,  $t > 1.5$  s).

## Analysis of the Scattered Waves

### Scattered Waves Arriving at a Trough

#### *Frequency domain*

Figure 7 shows the scattered waves at the trough (point A) coming from each part of the ground surface at frequencies of (a) 0.5, (b) 2.0, and (c) 3.5 Hz. These frequencies were chosen because in figure 5 neither amplification nor deamplification can be seen in the frequency response at 0.5 Hz due to the long wavelength, and significant deamplification and amplification can be seen at 2.0 and 3.5 Hz, respectively. In this figure, the total scattered waves  $\hat{u}_{jm}^s$  in equation (18) and first- to third-order scattered waves  $\hat{u}_{jm}^{(\nu)}$ , ( $\nu = 1, 2, 3$ ) in equation (17) are shown ( $j$ -th node corresponds to point A). Since the values of the scattered waves in the frequency domain are complex, we plotted their real and imaginary parts on the horizontal position of the source node ( $m$ -th node in equation (17) or equation (18)) where the scattered waves were generated. To examine the interferences between the incident wave and the scattered waves, we plotted real and imaginary parts other than the complex modulus. For the same reason, the plotted real and imaginary parts are those at the time of  $t_0$  given by equation (24) (i.e., the arrival time of the maximum amplitude

of a harmonic incident wave at the reference point ( $j$ -th node)).

$$v_j = \exp(ik_\beta z_j + i\omega t_0) = 1 \quad (24)$$

In figures 7a to c, we observe that the total scattered waves have similar shapes to those of the first-order scattered waves, so we can examine the characteristics of the total scattered waves based on the first-order ones. The first-order scattered waves consist mainly of the contribution coming from the slope of the convex part (indicated by 1 in the figure) and around point A on the concave part (indicated by 2). The former contribution from point 1 is positive for (a) 0.5 Hz and (c) 3.5 Hz, whereas the value is negative for (b) 2.0 Hz; the changes in the frequency response at point A shown in figure 5 can be understood as a result of this difference in the sign. Because the inclination factors at these source nodes for reference point A are positive (the inclination factor is frequency-independent), these changes are caused by the propagation of the scattered waves. This can be verified by the following simple calculation:

$$L/\lambda \sim \begin{cases} 1/2 & \text{for (b) 2.0 Hz} \\ 1 & \text{for (c) 3.5 Hz,} \end{cases} \quad (25)$$

where  $L$  is the propagation distance (distance between the source point and the reference point plus vertical distance between them—approximately 28 m), and  $\lambda$  is the wavelength of seismic waves.

The real parts of the scattered waves from point 2 have large negative values at all three frequencies, and the imaginary parts are relatively small at low frequency (e.g., 0.5 Hz). Taking

into account that the source nodes of these scattered waves are close to reference point A, and their inclination factors for point A are negative, the large real parts and the small imaginary parts can be considered to be a result of the short propagation distance of the scattered waves from the source nodes to point A. This short propagation distance also causes the low frequency-dependence of the scattered waves because changes of phase angles will not occur for such a short propagation distance except for extremely high-frequency components.

#### *Time domain*

Figure 8 plots waveforms of the scattered waves emanating from each part of the ground surface (source node) and observed at point A. The waveforms are plotted on the horizontal position of the source node. Here, (a) shows the total scattered waves, and (b) to (d) show the first- to third-order scattered waves. The response at point A shown in figure 6 is also plotted at the top of the figure.

In figure 8a, we can observe that the features we pointed out in figure 6 on the response at point A—i.e., the bend after the peak (indicated by 1 on the waveform) and the smaller peak amplitude (indicated by 2)—can be attributed to the arrivals of the scattered waves. That is, (1) the bend after the peak can be attributed to the scattered waves coming from the slope of the convex part facing point A (indicated by 1 on the ground model shown to the left side of the vertical axis). (2) The decrease in the peak amplitude is caused by the scattered waves coming from the ground

surface close to point A (indicated by 2 on the ground model). This is because the scattered waves arrive almost at the same time and have negative polarity to that of the incident wave. In regard to (1), we have pointed out that the frequency components of the scattered waves from point 1 are frequency-dependent; however, the waveform of the scattered wave from point 1 maintains the shape of the incident wave. This is further evidence that this frequency-dependency is mainly caused by changes in the phase angles due to the propagation of the scattered waves.

By comparing figures 8a to d, we can observe that the first-order scattered waves dominate the other higher-order ones. Therefore, the features of the total scattered waves can largely be examined based only on the first-order scattered waves, as mentioned in the previous section. The first-order scattered waves coming from the slope of the convex part (point 1) have positive polarity and time delays. Considering equation (14), it is well understood that the positive polarity is due to the positive inclination factor at the source node for point A, and the delays are primarily caused by the wave propagation from the source nodes to point A. The scattered waves from the nearby surface (point 2) can also be attributed to short distance  $r$  and the negative inclination factor  $\partial r / \partial \mathbf{n}(\mathbf{X})$ . It is noteworthy that the polarity does not depend on the wavelength (or predominant frequency) of the incident wave. The sign of the frequency response, of course, does depend on it because the sign of  $h_{jm}$  depends not only on the inclination factor but also on  $H_1^{(2)}(k_\beta r)$ . However, the changes in the value of  $H_1^{(2)}(\cdot)$  give the time delay and geometrical attenuation of a secondary wavelet due to wave propagation and do not flip the polarity of the secondary wavelet.

Generally, the changes in a raw spectrum can affect both the amplitude (and polarity) and the arrival time, and these effects can easily be examined in a time-domain analysis. This is one of the reasons we conducted the time-domain analysis in addition to the frequency-domain analysis.

Figures 10a and b show the total and the first-order scattered waves arriving at point A for the incident wave with the double-triangular time function of  $T = 0.07$  s (the characterized frequency is 3.5 Hz), respectively. The time function and its spectrum are shown in figure 9. In figure 10, we can observe that (1) the first-order scattered waves emanating from the slope of the convex part (indicated by 1) have a positive polarity and a time delay, (2) the first-order scattered waves emanating from the nearby surface (indicated by 2) have a negative polarity, and (3) the distortion in the total response shown in the top of the figure can be attributed to those scattered waves. These findings are the same as those pointed out in figure 8, so we can estimate that our explanations for figure 8 hold for the incident waves with other characterized frequencies.

Thus, the Neumann series expansion can reveal the excitation process of the complicated seismic response observed on ground surfaces with irregular topography by decomposing the response into an incident wave and scattered waves.

## Scattered Waves Arriving at a Peak

Point B is located at the peak of the sinusoidal ground model and represents mountains or areas with higher elevations. This point is very interesting, as shown in figure 5, because the frequency response at this point is higher over a wide frequency range compared to those at other ground surface areas.

Figure 11 shows the waveforms of the scattered waves in the same manner as in figure 8. In figure 11, we can see that the waveforms of the total and first-order scattered waves from this part (indicated by 1) have positive polarity, and their peak amplitudes appear almost at the same time as that of the incident wave. Their large peak amplitudes and the timing can be attributed to short distance  $r$  between points B and 1 for the same reason discussed in the previous section for point A. The positive polarity is due to the positive inclination factor around point B (see Fig. 2b).

Thus, these scattered waves always have positive polarity, so they always enhance the amplitude of the response at the peak due to constructive interference no matter what impinging occurs from incident waves. This is an explanation for amplified seismic responses observed at a peak from the viewpoint of the contribution of scattered waves.

In figure 11a, we can also observe the total scattered waves from the flank of the convex part on the left (indicated by 2) as well as the flat areas (indicated by 3); the former implies the propagation of the scattered waves beneath the trough (indicated by 4). This observation highlights

that diffraction has to be considered in discussions on seismic response at ground surfaces with irregular topography.

### **Scattered Waves Arriving at a Flat Area**

Point C is located on the flat area next to the edge of the sinusoidal part. Figure 12 shows the waveforms of the scattered waves. In figure 12, we observe significant scattered waves with a negative polarity from the edge of the irregular surface (indicated by 1), and an abrupt decay in their amplitudes along the irregular surface (indicated by 2). As depicted in the ground model in figure 12, this abrupt change can be explained by the change in the inclination factor. That is, the inclination factor at the edge of the irregular part is significant because of the relatively small angle (approximately  $\pi/4$  rad) between the normal direction at this part,  $\mathbf{n}$ , and  $\mathbf{Y} - \mathbf{X}$  (the direction from the source node to reference point C). This angle increases (therefore, the inclination factor decreases) abruptly if the source node  $\mathbf{X}$  moves along the irregular surface toward the peak (point B).

We can observe in figure 12 scattered waves from point 3 and diffracted waves from the flank of the convex part on the left side (indicated by 4) as mentioned in the previous sections. On the contrary, no significant scattered waves can be seen from the flat areas (indicated by 5) because the flat areas can affect point C only by multiple (second- or higher-order) scattering due to their

zero-inclination factors for reference point C.

## Conclusion

We analyzed scattered waves induced by ground surface irregularities and examined the excitation process of the complicated seismic response of the ground. The major conclusions of this study are enumerated as follows:

- 1) The contribution of the scattered waves was formulated based on the BEM and Neumann series expansion. By using this method, the surface response of the ground can be decomposed into an incident wave and scattered waves in the order that represents the number of reflections at the ground surface.
- 2) The mathematical expression of the first-order scattered waves consists of the inclination factor and the wave function of secondary wavelets, which is similar to that of the Huygens-Fresnel principle. The inclination factor is simply given by the term  $\partial r / \partial n$ , and it is an effective index to evaluate the amplitude of scattered waves.

In the numerical analysis using a sinusoidal ground model, we pointed out the following:

- 3) The first-order scattered waves dominate the other higher-order ones; therefore, we can investigate the characteristics of the total scattered waves based only on the property of the first-order scattered waves.

- 4) At the trough (point A in Fig. 3), the contribution of the first-order scattered waves consists mainly of the contribution from point 1 in figure 7 (the slope of the convex part facing the reference point) and point 2 (around the reference point on the concave part). The former scattered waves from point 1 have positive polarity because of the positive inclination factor and appear much later than the arrival of the incident wave due to wave propagation from the source points. In contrast, the latter from point 2 have negative polarity because of the negative inclination factor, and appear almost at the same time as the arrival of the incident wave because of the short propagation distance. Therefore, the scattered waves from point 2 always cause destructive interference with the incident wave at a trough.
- 5) At the peak of the mountain (point B in Fig. 3), large-amplitude first-order waves scattered from a nearby surface are observed. These scattered waves have positive polarity and appear almost at the same time as the arrival of the incident wave because of the positive inclination factor and the short propagation distance. Therefore, the scattered waves from this part always cause constructive interference with the incident wave at a peak.

In this study, we have conducted the analyses only in an SH wavefield in a homogeneous Earth model because of its simplicity and similarity between the phenomena in SH and P-SV wavefields (Bouchon, 1973). However, similar considerations in the P-SV wavefield are obviously needed. The major differences between the SH and P-SV wavefields are the existence of phase conversions and the Rayleigh waves, and these effects will also distort the wavefield. Furthermore,

the existence of the Rayleigh wave will affect the formulation of the method presented in this study because the method is based on the perturbations of a BEM-matrix from a ground with a flat surface (i.e.,  $E$  in equation (15) should be a nondiagonal matrix for the analysis in the P-SV wavefield).

Obviously, a homogeneous Earth model is an oversimplification. The effect of structural heterogeneities will influence the distortion of the wavefield, and detailed discussions on this are needed. However, the existence of the wave conversion and the Rayleigh waves in a ground with structural heterogeneities will distort the wavefield more significantly than in the P-SV wavefield in a homogeneous medium. Thus, the distortion of the P-SV wavefield and a wavefield in a heterogeneous Earth model are much complicated and will be the subjects of future study.

**Acknowledgments:** This study was conducted under the sponsorship of JNES (Japan Nuclear Energy Safety Organization) open application research project for enhancing the basis of nuclear safety. The authors deeply appreciate their support. The authors are also grateful to the anonymous reviewers for their valuable suggestions on improving the manuscript.

## REFERENCES

- Aki, K. and K. L. Larner (1970). Surface motion of a layered medium having an irregular interface due to incident plane SH waves, *J. Geophys. Res.*, **75**, **5**, 933–954.
- Aki, K. (1989). Local site effects on ground motion, *Earthquake Engineering and Soil Dynamics* **2**, *Recent advances in ground-motion evaluation*, ASCE, 103–155.
- Bard, P.-Y. (1982). Diffracted waves and displacement field over two-dimensional elevated topographies, *Geophys. J.R. astr. Soc.*, **71**, 731–760.
- Boore, D. M. (1972). A note on the effect of simple topography on seismic SH waves, *Bull. Seism. Soc. Am.*, **62**, **1**, 275–284.
- Boore, D. M. (1973). The effect of simple topography on seismic waves: implications for the accelerations recorded at Pacoima dam, San Fernando valley, California, *Bull. Seism. Soc. Am.*, **63**, **5**, 1603–1609.
- Bouchon, M. (1973). Effect of topography on surface motion, *Bull. Seism. Soc. Am.*, **63**, **3**, 615–632.
- Bouchon, M., C. A. Schultz, and M. N. Toksoz (1996). Effect of three-dimensional topography on seismic motion, *J. Geophys. Res.*, **101**, **B3**, 5835–5846.
- Brebbia, C. A. and S. Walker (1980). *Boundary element techniques in engineering*, Butterworth & Co. Ltd.

- Frazer, L. N. and J. B. Sinton (1984). A Kirchhoff method for the computation of finite-frequency body wave synthetic seismograms in laterally inhomogeneous media, *Geophys. J. R. astr. Soc.*, **78**, 413–429.
- Fu, L-Y. (2005). Rough surface scattering: comparison of various approximation theories for 2D SH waves, *Bull. Seism. Soc. Am.*, **95**, **2**, 646–663.
- Fujiwara, H. and H. Takenaka (1994). Calculation of surface waves for a thin basin structure using a direct boundary element method with normal modes, *Geophys. J. Int.*, **117**, 69–91.
- Geli, L., P. Bard, and B. Jullien (1988). The effect of topography on earthquake ground motion: a review and new results, *Bull. Seism. Soc. Am.*, **78**, **1**, 42–63.
- Hatayama, K. and H. Fujiwara (1998). Excitation of secondary Love and Rayleigh waves in a three-dimensional sedimentary basin evaluated by the direct boundary element method with normal modes, *Geophys. J. Int.*, **133**, **2**, 260–278.
- Hecht, E. (2002). *Optics*, 4th Ed., Pearson Education Inc., Translated by Ozaki, Y. and Asakura, T., Maruzen Co., LTD., 2003.
- Hudson, J. A. and J. R. Heritage (1981). The use of the Born approximation in seismic scattering problems, *Geophys. J. R. astr. Soc.*, **66**, 221–240.
- Kato, T. (1980). *Perturbation theory for linear operators*, 2nd Ed., Springer-Verlag.
- Kawase, H. (1988). Time-domain response of a semi-circular canyon for incident SV, P, and Rayleigh waves calculated by the discrete wavenumber boundary element method, *Bull.*

- Seism. Soc. Am.*, **78**, **4**, 1415–1437.
- Kennet, B. L. N. (1972). Seismic waves in laterally inhomogeneous media, *Geophys. J. R. astr. Soc.*, **27**, 301–325.
- Kobayashi, S. (1985). Fundamentals of boundary integral equation methods in elastodynamics, *Topics in boundary element research, Vol. 2, Time-dependent and vibration problems*, Brebbia, C. A.(editor), Springer-Verlag.
- Koketsu, K. and H. Takenaka (1989). Theories on wave propagation in the near field of seismic sources, *Zisin*, **2**, **42**, **3**, 391–403 (in Japanese).
- Mogi, H., H. Kawakami, and K. Fukuhara (2005). Boundary element-perturbation method using Neumann series expansion for seismic response analysis of the ground with irregular surface, *J. Struct. Mech. Earthquake Eng.*, JSCE, **787/I-71**, 81–90 (in Japanese).
- Ohtsuki, A. and K. Harumi (1983). Effect of topography and subsurface inhomogeneities on seismic SV waves, *Earthq. Engng. Struct. Dyn.*, **11**, 441–462.
- Reinoso, E., L. C. Wrobel, and H. Power (1997). Three-dimensional scattering of seismic waves from topographical structures, *Soil Dyn. Earthq. Engng.*, **16**, 41–61.
- Sanchez-Sesma, F. J., I. Herrera, and J. Aviles (1982). A boundary method for elastic wave diffraction: application to scattering of SH waves by surface irregularities, *Bull. Seism. Soc. Am.*, **72**, **2**, 275–284.
- Sanchez-Sesma, F. J. (1985). Diffraction of elastic SH waves by wedges, *Bull. Seism. Soc. Am.*,

75, 5, 1435–1446.

Sanchez-Sesma, F. J. and M. Capillo (1991). Diffraction of P, SV, and Rayleigh waves by topographic features: a boundary integral formulation, *Bull. Seism. Soc. Am.*, **81**, 6, 2234–2253.

Scott, P. and D. Helmberger (1983). Applications of the Kirchhoff-Helmholtz integral to problems in seismology, *Geophys. J. R. astr. Soc.*, **72**, 237–254.

Zhang, R. and M. Shinozuka (1996). Effects of irregular boundaries in a layered half-space on seismic waves, *J. Sound and Vibration*, **195**, 1, 1-16.

Author affiliations:

Hidenori Mogi

Department of Civil and Environmental Engineering, Saitama University

255 Shimo-ohkubo Sakura-ku Saitama-shi Saitama 338-8570, Japan

hmogi@kiban.civil.saitama-u.ac.jp

Hideji Kawakami

Geosphere Research Institute of Saitama University

255 Shimo-ohkubo Sakura-ku Saitama-shi Saitama 338-8570, Japan

## List of Figures

Figure 1 Irregular half-space and coordinate system

Figure 2 Sign of inclination factor  $\partial r/\partial n$  for ground that is (a) concave and (b) convex.

Figure 3 The sinusoidal ground model used in this study with the location of reference points A, B, and C.

Figure 4 (a) Time function and (b) spectrum of the incident wave used in this study. The characterized frequency of the incident wave is 1.25 Hz.

Figure 5 Frequency-response functions at the reference points induced by a vertical incident wave (Mogi *et al.*, 2005). The three frequencies shown here were chosen for the frequency-domain analysis of the scattered waves.

Figure 6 Waveforms induced by a vertical incident wave with double-triangular time function. The characterized frequency of the incident wave is 1.25 Hz.

Figure 7 Total scattered wave  $\hat{u}_{jm}^s$  and first- to third-order scattered waves  $\hat{u}_{jm}^{(\nu)}$ , ( $\nu = 1, 2, 3$ ) at point A for frequencies (a) 0.5, (b) 2.0 and (c) 3.5 Hz (Mogi *et al.*, 2005).

Figure 8 Waveforms of the scattered waves emanating from each part of the ground surface

(source node) and arriving at point A. Waveforms are plotted on the horizontal position of the source node where the scattered wave emanates from. In these figures, (a) shows the total scattered waves, and (b) to (d) show the first- to third-order scattered waves, respectively. The response at point A shown in figure 6 is also plotted at the top of the figure. The characterized frequency of the incident wave is 1.25 Hz.

Figure 9 (a) Time function and (b) spectrum of the incident wave with  $T = 0.07$  s (characterized frequency is 3.5 Hz).

Figure 10 Waveforms of (a) total and (b) first-order scattered waves arriving at point A. The characterized frequency of the incident wave is 3.5 Hz. The total response waveform at point A is also shown at the top of the figure in the same manner as in figure 8.

Figure 11 Waveforms of (a) total and (b) first-order scattered waves arriving at point B. The total response waveform at point B is also shown at the top of the figure in the same manner as in figure 8. The characterized frequency of the incident wave is 1.25 Hz.

Figure 12 Waveforms of (a) total and (b) first-order scattered waves arriving at point C. The total response waveform at point C is also shown at the top of the figure in the same manner as in figure 8. The characterized frequency of the incident wave is 1.25 Hz.

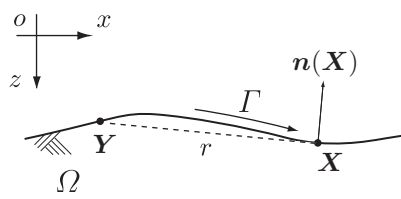


Figure 1. Irregular half-space and coordinate system

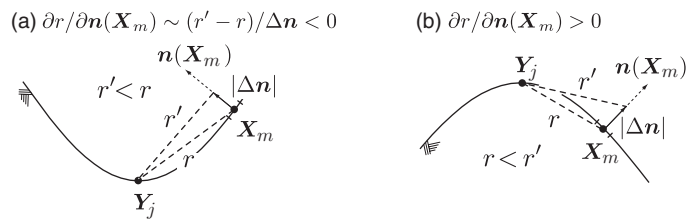


Figure 2. Sign of inclination factor  $\partial r / \partial n$  for ground that is (a) concave and (b) convex.

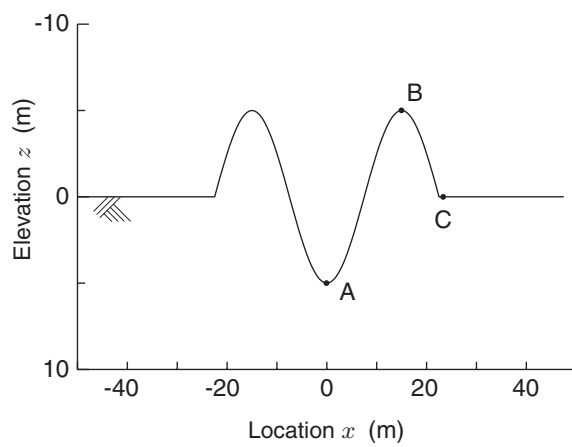


Figure 3. The sinusoidal ground model used in this study with the location of reference points A, B, and C.

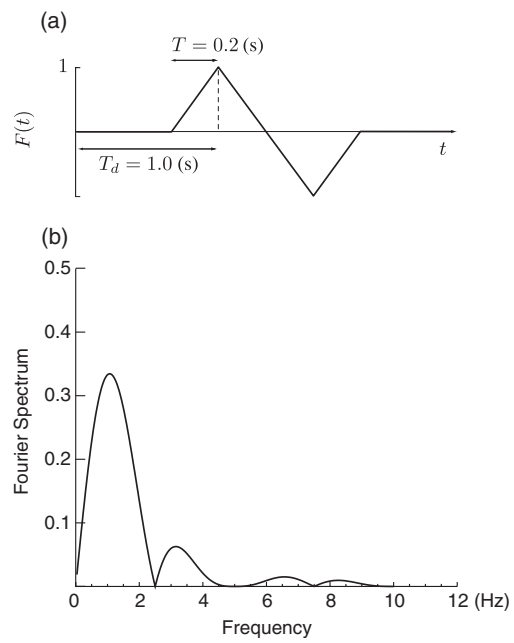


Figure 4. (a) Time function and (b) spectrum of the incident wave used in this study. The characterized frequency of the incident wave is 1.25 Hz.

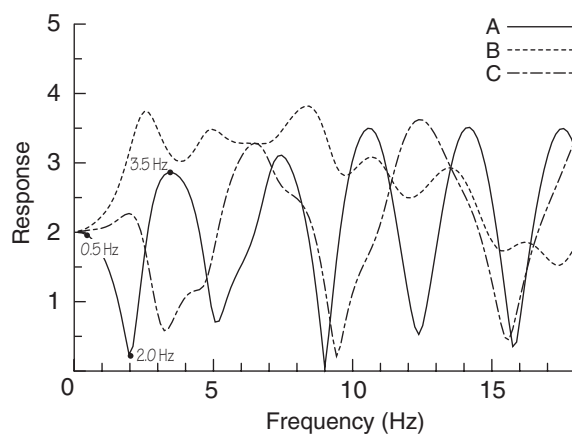


Figure 5. Frequency-response functions at the reference points induced by a vertical incident wave (Mogi *et al.*, 2005). The three frequencies shown here were chosen for the frequency-domain analysis of the scattered waves.

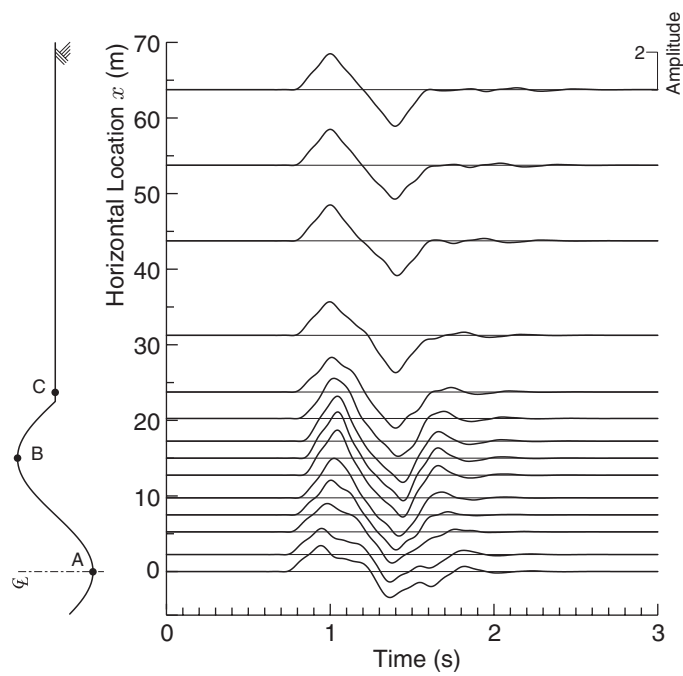


Figure 6. Waveforms induced by a vertical incident wave with double-triangular time function. The characterized frequency of the incident wave is 1.25 Hz.

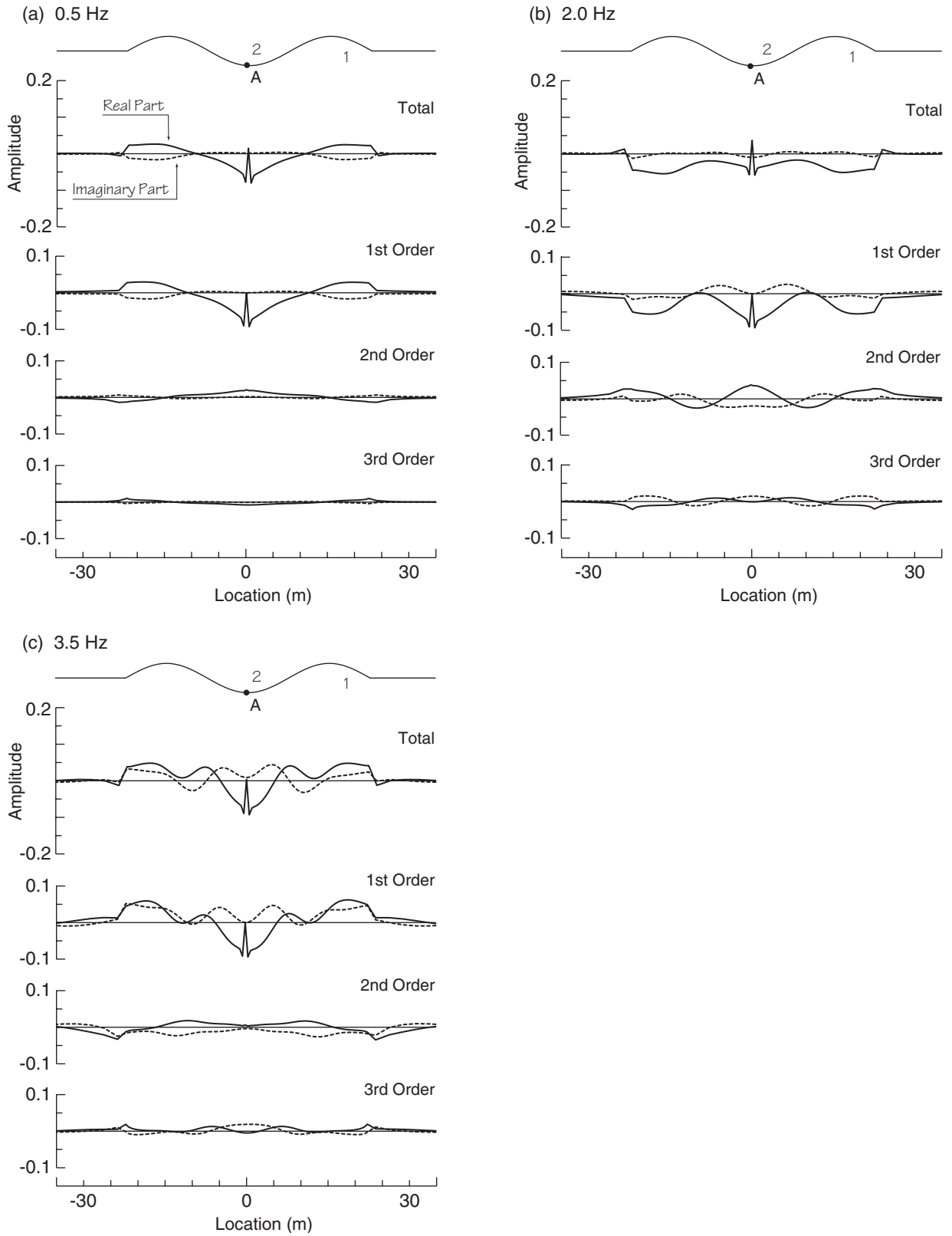


Figure 7. Total scattered wave  $\hat{u}_{jm}^s$  and first- to third-order scattered waves  $\hat{u}_{jm}^{(\nu)}$ , ( $\nu = 1, 2, 3$ ) at point A for frequencies (a) 0.5, (b) 2.0 and (c) 3.5 Hz (Mogi *et al.*, 2005).

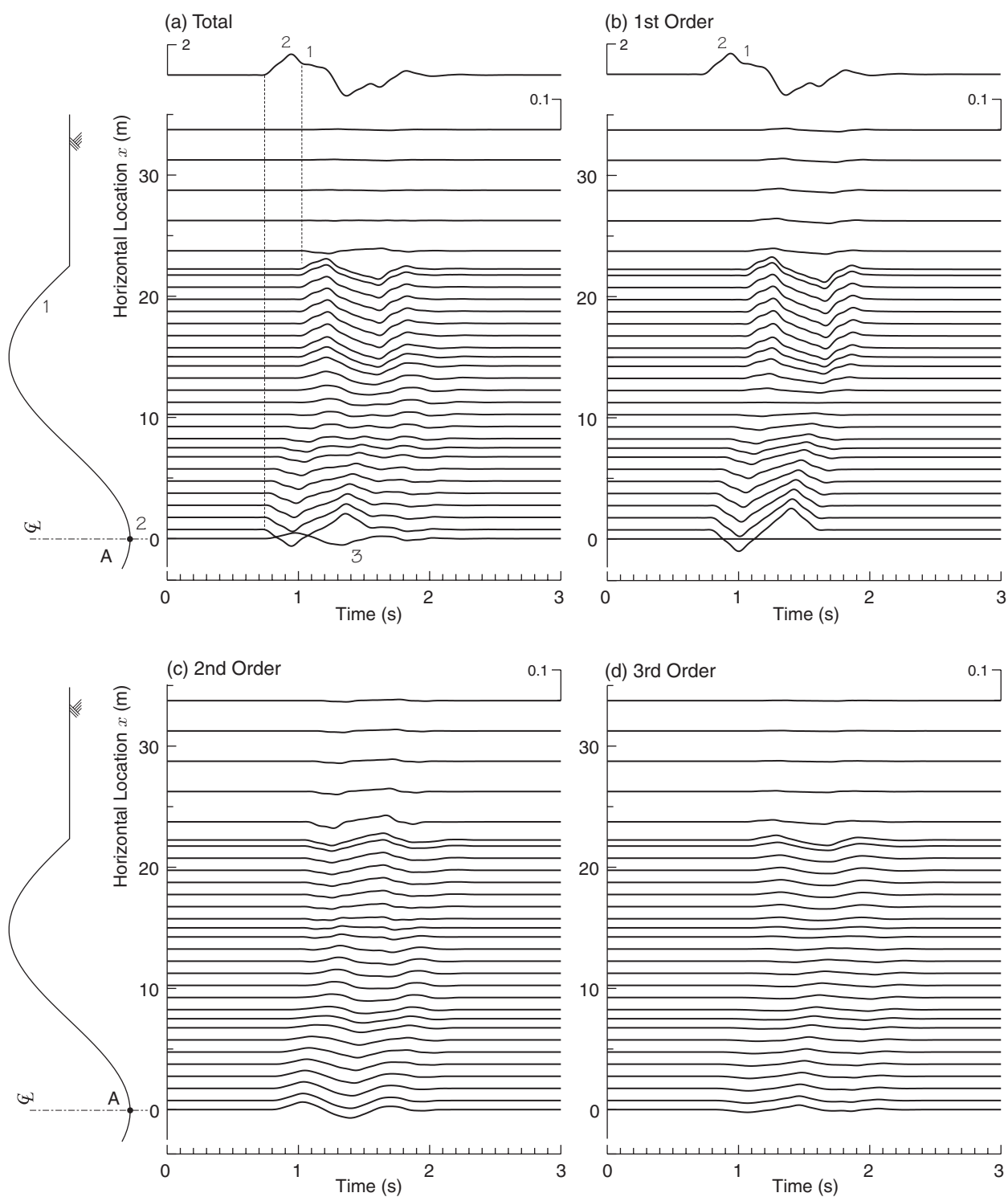


Figure 8. Waveforms of the scattered waves emanating from each part of the ground surface (source node) and arriving at point A. Waveforms are plotted on the horizontal position of the source node where the scattered wave emanates from. In these figures, (a) shows the total scattered waves, and (b) to (d) show the first- to third-order scattered waves, respectively. The response at point A shown in figure 6 is also plotted at the top of the figure. The characterized frequency of the incident wave is 1.25 Hz.

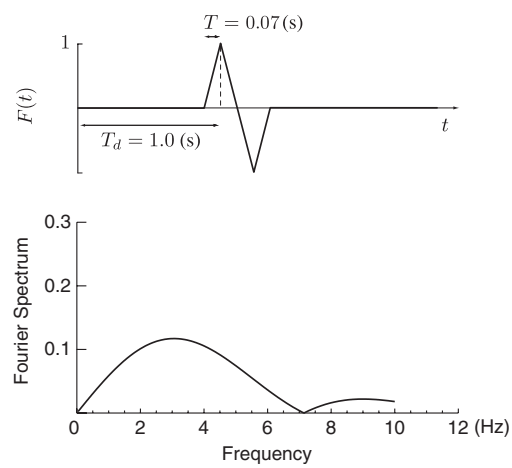


Figure 9. (a) Time function and (b) spectrum of the incident wave with  $T = 0.07$  s (characterized frequency is 3.5 Hz).

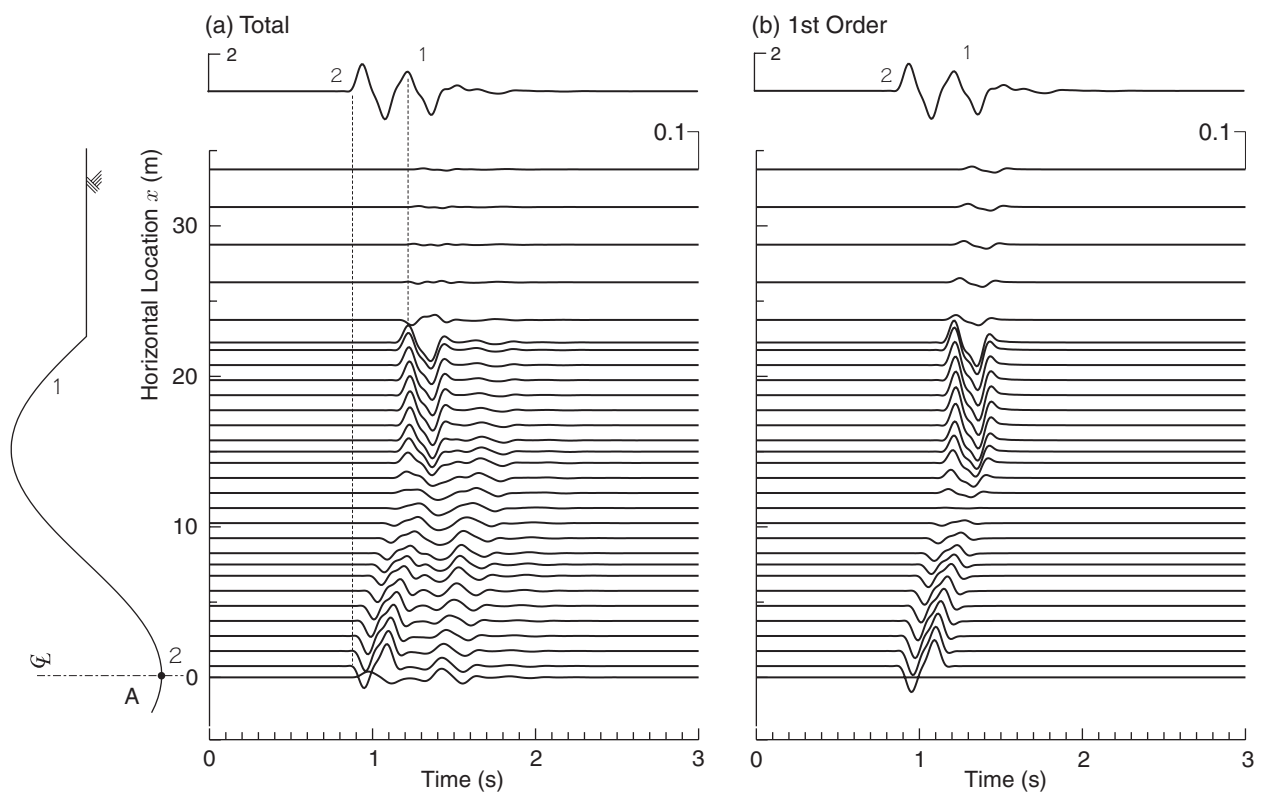


Figure 10. Waveforms of (a) total and (b) first-order scattered waves arriving at point A. The characterized frequency of the incident wave is 3.5 Hz. The total response waveform at point A is also shown at the top of the figure in the same manner as in figure 8.

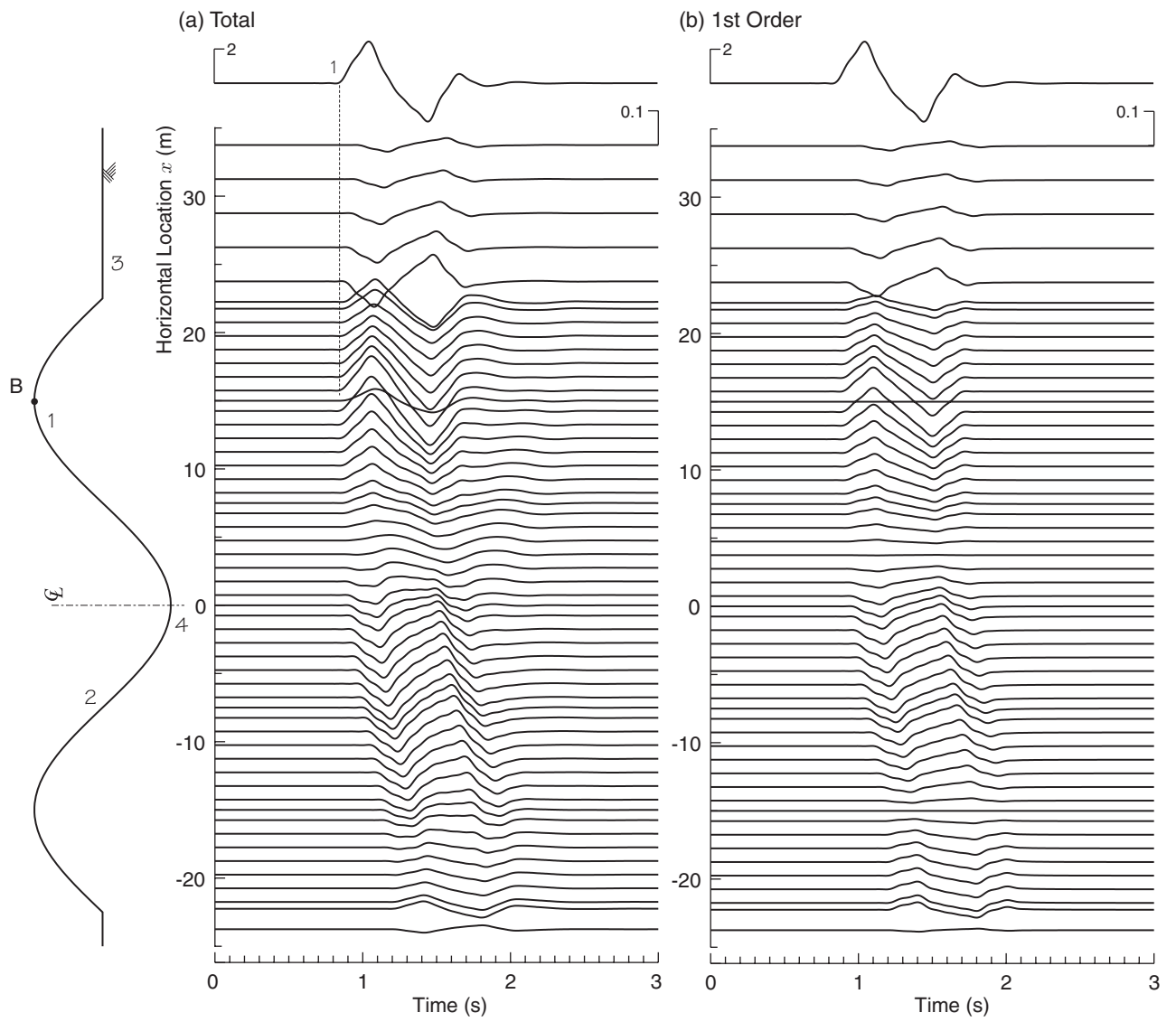


Figure 11. Waveforms of (a) total and (b) first-order scattered waves arriving at point B. The total response waveform at point B is also shown at the top of the figure in the same manner as in figure 8. The characterized frequency of the incident wave is 1.25 Hz.

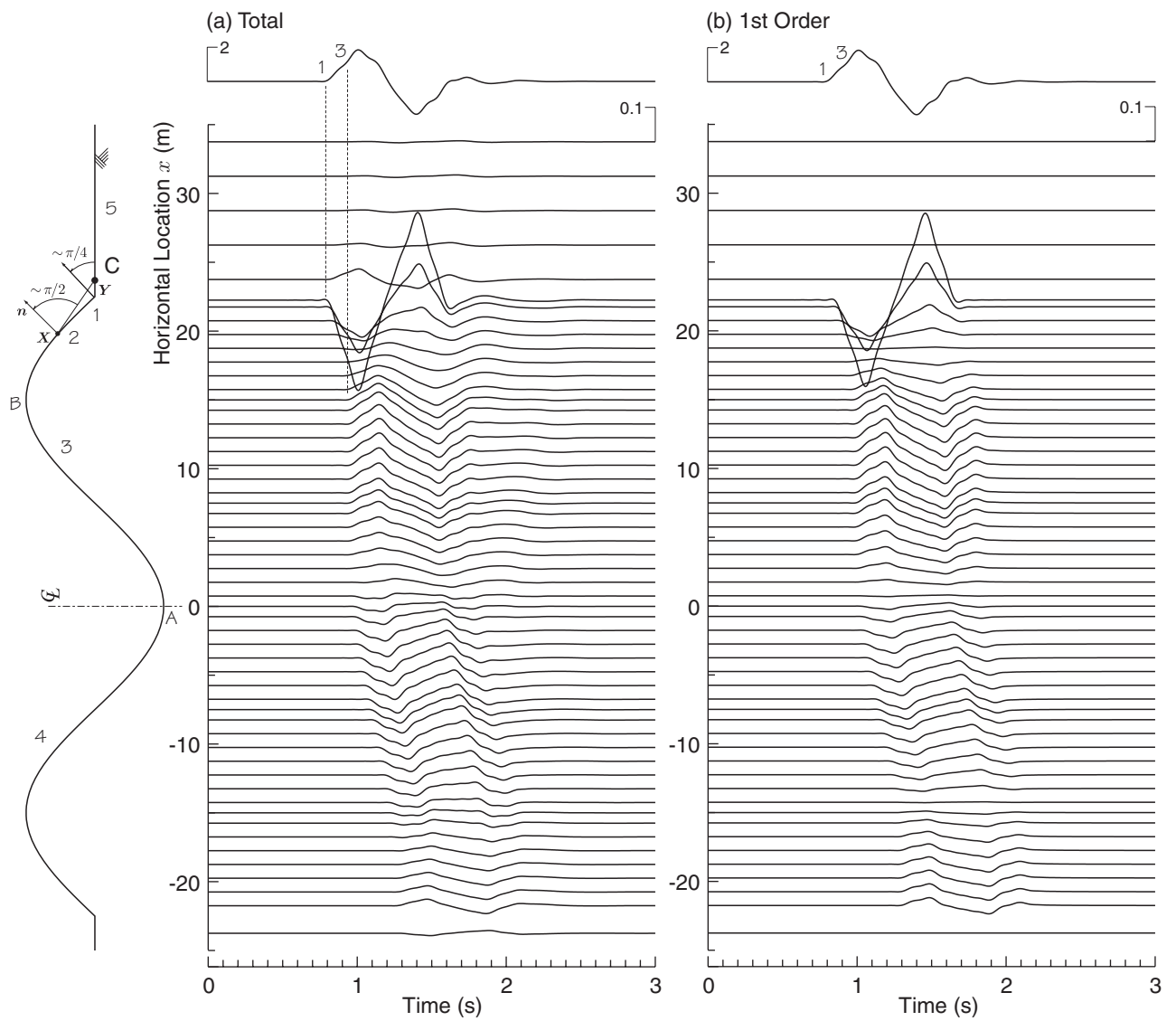


Figure 12. Waveforms of (a) total and (b) first-order scattered waves arriving at point C. The total response waveform at point C is also shown at the top of the figure in the same manner as in figure 8. The characterized frequency of the incident wave is 1.25 Hz.